



Lithium ion battery electrode manufacturing model accounting for 3D realistic shapes of active material particles

Jiahui Xu ^{a,b}, Alain C. Ngandjong ^{a,b}, Chaoyue Liu ^{a,b}, Franco M. Zanotto ^{a,b}, Oier Arcelus ^{a,b}, Arnaud Demortière ^{a,b,c}, Alejandro A. Franco ^{a,b,c,d,*}

^a Laboratoire de Réactivité et Chimie des Solides (LRCS), UMR CNRS 7314, Université de Picardie Jules Verne, Hub de l'Energie, 15 rue Baudelocque, 80039 Amiens Cedex, France

^b Réseau sur le Stockage Electrochimique de l'Energie (RS2E), FR CNRS, 3459, 15 rue Baudelocque, 80039 Amiens Cedex, France

^c ALISTORE-European Research Institute, FR CNRS 3104, 15 rue Baudelocque, 80039 Amiens Cedex, France

^d Institut Universitaire de France, 103 Boulevard Saint Michel, Paris, 75005, France

HIGHLIGHTS

- Model for electrode manufacturing accounts for real particle shapes.
- Particle shapes are extracted from X-ray computed tomography of real electrodes.
- Deformation and rotation of particles is observed upon calendering.
- Electrode tortuosity is better described with real particle shapes than with spheres.

GRAPHICAL ABSTRACT



ARTICLE INFO

Keywords:
Lithium ion battery
Electrode manufacturing
Computational modeling
Digital twin

ABSTRACT

The demand for lithium ion batteries (LIBs) in the market has gradually risen, with production increasing and expected to be boosted through the massive emergence of gigafactories. To meet industrial needs, the development of digital twins designed to accelerate the optimization of LIB manufacturing processes is essential. We report here a new three-dimensional physics-based modeling workflow able to predict the influence of manufacturing parameters on the electrode microstructure. This novel modeling workflow accounts for real active material particle shapes obtained from X-ray micro-computed tomography, upgrading our previous models where the particles were considered to be spherical. The modeling workflow is supported on Coarse-Grained Molecular Dynamics simulating the slurry, its drying and the calendering of the electrode resulting from the drying simulation. This model enables to link the manufacturing parameters with the real microstructure of the electrodes and to better observe the effect of the former on the heterogeneity of the electrodes. By using as user case electrodes containing $\text{LiNi}_{0.33}\text{Co}_{0.33}\text{Mn}_{0.33}\text{O}_2$ as active material, the simulations allow us, among others, to observe the alteration of the electrode heterogeneity during the manufacturing process and the deformation of the secondary particles of active material.

* Corresponding author. Laboratoire de Réactivité et Chimie des Solides (LRCS), UMR CNRS 7314, Université de Picardie Jules Verne, Hub de l'Energie, 15 rue Baudelocque, 80039 Amiens Cedex, France.

E-mail address: alejandro.franco@u-picardie.fr (A.A. Franco).

GLOSSARY

LIBs	lithium ion batteries
NMC111	$\text{LiNi}_{0.33}\text{Co}_{0.33}\text{Mn}_{0.33}\text{O}_2$
CBD	carbon binder domain
XCT	X-ray computed tomography
AM	active material
NMC	$\text{LiNi}_x\text{Mn}_y\text{Co}_{1-x-y}\text{O}_2$
NMP	N-Methyl-2-pyrrolidone
LFP	LiFePO_4
LCO	LiCoO_2
CGMD	coarse-grained molecular dynamics
DEM	discrete element method
PVdF	polyvinylidene fluoride
FF	force fields
LJ	Lennard-Jones
JKR	Johnson-Kendall-Roberts
CC	current collector
PNM	pore network model

1. Introduction

Rechargeable lithium ion batteries (LIBs) are widely used in mobile electronics, military, medical and electric public transport, and now account for a growing share of the private vehicle market [1]. In recent years, the production of LIBs has gradually expanded and it is expected to increase even more with the massive emergence of gigafactories designed to fulfill the demands of the automotive sector [2]. In response to market demands, studies have concentrated on achieving higher energy densities while maintaining or reducing costs [3,4].

In LIBs, the electrode is where the electrochemical lithium (de-)insertion reaction takes place and its complex architecture affects the rate and degree of the reaction. In order to optimize the performance of LIBs, it is essential to understand the influence of each parameter at each stage of the manufacturing on the electrode architectures. In general, the properties of the electrode slurry (e.g. density, viscosity) impact the coating process, which is related to the size and shape of the material, relative ratio of components and the mixing conditions [5–8]. The evaporation of the solvent affects the architecture of the dried electrode, during which the carbon binder domain (CBD) and the percolated porous structure are formed [9,10]. The calendering process, a critical step in the manufacturing, reduces the electrode thickness, enhancing electrical conductivity, thermal conductivity and energy density, at the expense of reducing the porosity and altering ionic conductivity [11–13]. In addition, the effect of mechanical deformation of the electrode in the electrochemical reactions taking place in it should also be considered in the preparation process [14]. Non-destructive techniques, such as X-ray computed tomography (XCT), are widely used to characterize the microstructure of the electrodes, enabling volume-based three-dimensional (3D) characterization. This approach has been used to investigate the porosity and tortuosity factor of a significant number of anode and cathode electrodes with different active materials (AMs), including graphite, $\text{LiNi}_x\text{Mn}_y\text{Co}_{1-x-y}\text{O}_2$ (NMC), LiFePO_4 (LFP) and LiCoO_2 (LCO) [15]. However, the study of CBD distribution in the electrode is limited due to the nano-features and the similarities in X-ray attenuation coefficients of carbon and pores. In order to overcome the deficiencies of neglecting the CBD, Zielke et al. developed a combination of X-ray tomography and a virtual design approach [17]. Lu et al. combined separate scans of high-attenuating NMC and low-attenuating CBD, which enabled to reconstruct the 3D electrode including microstructural heterogeneities at the nanoscale [16]. Nguyen et al. used X-Ray holographic nano-tomography to distinguish CBD in the NMC electrode [18]. In order to unveil the evolution of electrode

architectures, several convolutional neural network-based image segmentation methods have been also developed to try to improve the 3D imaging and discrimination between phases [19,20].

In our previous work in the context of our ARTISTIC project [21], coarse-grained molecular dynamics (CGMD) and discrete element method (DEM) were used to construct physical models able to simulate the different electrode manufacturing steps. These procedures ranged from the slurry, consisting of AMs, conductive carbon, binder and solvent [22], to the drying [23,24] and calendering [25] of the electrode by using NMC111 electrodes as an example. Likewise, models of the electrolyte infiltration by Lattice Boltzmann Method [26–28] and electrochemical performance assessment by continuum modeling [25,29] were also developed by us to achieve a digital twin of the manufacturing process of LIB cells. This digital twin allows to predict the influence of the manufacturing parameters (e.g. formulation, degree of compression) on the electrode 3D microstructures (previously called by us *meso-structures*) and their associated properties (e.g. porosity, tortuosity factor, the spatial distribution of the materials). By combining this physics-based digital twin with machine learning and Bayesian Optimization, we have shown that it is possible to predict which manufacturing parameters to adopt in order to optimize different electrode properties simultaneously [30,31]. In the ARTISTIC models reported until now, spherical particles have been utilized to represent the AM and the CBD, which may differ from real electrodes. In another approach, Nikpour et al. [32] generated a multi-phase smoothed particles model, simulating the drying and calendering process by using non-spherical AM particles. However, in their approach the particle morphology is generated from 2D SEM images, which limits the representativity of the real particle shapes in 3D. Furthermore, works have reported that aspherical particles lead to nonuniform lithiation during electrochemical reactions [33].

Here, we report a significant upgrade of our ARTISTIC project manufacturing models that, for the first time, account for the real 3D morphology of the AM particles. For demonstration purposes, we employ here the morphology of AM particles retrieved from the μ -XCT characterization of NMC111-based electrodes. In our new electrode manufacturing modeling workflow, the 3D volume of the NMC secondary particles is used to generate the input. The new AMs replace the original spherical particles with realistic shapes formed by spherical primary particles. This brings our model closer to the real electrode morphology, allowing us to capture the deformation of AM particles during calendering. The goal of the effort described in this article is to incorporate realistic particles into our pre-existing manufacturing simulation workflow and to study the changes in electrode microstructure upon formulation change and calendering degree, with a 1-to-1 comparison with μ -XCT results.

This article is organized as follows: we first describe the procedures for electrode preparation, tomography characterization and associated data processing; we then detail our new manufacturing simulation workflow accounting for real active material particle shape; then we discuss the results and finally we conclude and indicate future perspectives for this work.

2. Materials and methods

2.1. Sample preparation and properties measurement

$\text{LiNi}_{0.33}\text{Co}_{0.33}\text{Mn}_{0.33}\text{O}_2$ -written as NMC111 in the following- (Umicore), carbon black (C-NERGY™ super C65) and Polyvinylidene fluoride (PVdF) (Solef™ 5130/1001, Solvay) are premixed in a given ratio overnight. Afterwards, N-Methyl-2-pyrrolidone (NMP) is added until reaching the desired solid content: 60% dry mass ratio for 94:3:3 AM/carbon/binder weight ratio and 69% dry mass ratio for 96:2:2 AM/carbon/binder weight ratio. The mixture is performed in a Dispermat CV3-PLUS high-shear mixer for 2 h in a water-bath cooled recipient at 25 °C. Then, the slurry is coated over a 22.5 μm thick Aluminum current

collector by using a comma-coater prototype-grade machine (PDL250, People & Technology, Korea) with a comma gap of 115 µm and 155 µm, respectively, and passes through two ovens with temperatures of 85 °C and 95 °C, in that order. After drying, the electrodes are calendered in a prototype-grade lap press calendar (BPN250, People & Technology, Korea), under various applied pressures and at constant line speed (0.54 m/min) at 60 °C.

The slurry densities are acquired by using a densimeter (DMA4500, Anton Paar GmbH). Porosities of the electrodes are calculated by the following Equation (1):

$$\phi = \left(1 - \frac{m_{\text{electrode}}}{V_{\text{electrode}}} * \sum_{i=1}^n \frac{x_i}{\rho_i} \right) * 100\% \quad (1)$$

where $m_{\text{electrode}}$ and $V_{\text{electrode}}$ stand for the mass and volume of the electrode respectively, x_i is the mass fraction of i in the solid and ρ_i is the density of the material. The porosities are measured on 13 mm diameter disks.

2.2. µ-XCT measurements and data processing

The µ-XCT measurements were carried out on the 96:2:2 electrodes both before and after the calendering process at the P05 synchrotron imaging beamline (Desy, Hamburg, Germany) [34], as detailed in a former paper from our group [26]. The electrodes of this formulation were used to extract particle morphology and validate the microstructure of the model outcome. The reconstructed data have been segmented into biphasic images (AM and pores + CBD) by using the machine learning segmentation plugin Trainable Weka [35] in ImageJ. The segmentation process employs the Fast Random Forest class, the features and parameters which are detailed in Table S1. The resulting 3D microstructure has an effective voxel size of 0.642 µm. The biphasic image stacks are imported into the commercial software package Avizo V9.4 (Avizo, Thermo Fisher Scientific, Waltham, Massachusetts, USA) [36] for post-treatment. The secondary particles in the uncalendered electrode are used to construct the particles dataset. One voxel on the surface of the AM phase is eroded to separate the connected large particles. The Watershed-based Object-Separate algorithm is used to label the individual particles. Following separation, one voxel is dilated back to maintain the particles' size.

2.3. Initial structure generation

The bounding box for each identified particle is then excised from the microstructure, and saved into a ‘particle database’ as Python serialized objects, along with some metadata, such as their volume equivalent sphere diameters. When building the physical model and establishing the initial structure, the particles are chosen randomly from the newly generated particle database while accounting for the PSD of the real electrode, until the target AM volume is obtained. In order to control the total number of particles in the physical model, preventing our CGMD simulations from getting computationally too costly, the original labeled particles are downsampled by taking every $2 \times 2 \times 2$ voxel³. Then, the CGMD model structure is prepared by substituting the downsampled voxels with spheres (primary AM particles) of equivalent volume, with a diameter of 1.59 µm. The secondary particles are randomly rotated and displaced before being placed into the simulation box to guarantee the unpredictability of the particles in the initial structure. The number of CBD is determined by the formulation. In this work, we simulated two formulations: 94% NMC - 3% C65 - 3% PVDF (94% AM and 6% CBD in the simulation) and 96% NMC - 2% C65 - 2% PVDF (96% AM and 4% CBD). The associated information about the initial structure is depicted in Fig. S1. We employ the same particle size distribution as the material powder to keep consistency with the real electrode, as illustrated in the Fig. S2.

2.4. Physical model development

The dynamic behavior of particles in the simulation box conforms to Newton's equations of motion. Although the particles in the CGMD model have a specific size and density, the kinetic calculations do not take the shape of the particle into account, but only the location of the center of mass of the primary particles. As such our new CGMD model of the electrode slurry and drying does not include the complex geometry of the secondary particles and the associated rotational degrees of freedom, which are typical features of DEM approaches. Thanks to the description of interactions between primary particles which allows capturing the interaction between secondary particles with complex geometries, our new CGMD model is a kind of DEM model in what it concerns the simulation of the calendering step.

There are two force fields (FFs) in use. The Lennard-Jones (LJ) FF derived from its corresponding potential as detailed in Equations (2) and (3) [37], describes the interaction between any two particles within the simulated box.

$$E_{\text{LJ}}(r) = 4\epsilon \left[\left(\frac{\sigma}{r} \right)^{12} - \left(\frac{\sigma}{r} \right)^6 \right] \quad r < r_c \quad (2)$$

$$F_{\text{LJ}}(r) = -\nabla E_{\text{LJ}}(r) \quad r < r_c \quad (3)$$

where r is the distance between the two particles. The Johnson-Kendall-Roberts (JKR) interaction is used between two particles that overlap each other, describing the normal and tangential forces that are expressed by Eq 4, 5, 6 and 7 [38]:

$$F_{\text{JKR},n} = \left(\frac{4Ea^3}{3R} - 2\pi a^2 \sqrt{\frac{4\gamma E}{\pi a}} \right) \mathbf{n} - \eta_n \mathbf{v}_{n,\text{rel}} \quad (4)$$

$$\eta_n = \eta_{n0} m_{\text{eff}} \quad (5)$$

$$F_{\text{JKR},t} = \min \left(\mu_t \left\| \left(\frac{4Ea^3}{3R} - 2\pi a^2 \sqrt{\frac{4\gamma E}{\pi a}} \right) \mathbf{n} + 6\pi\gamma R \right\|, \left\| -k_t a \xi + x_{\gamma,t} \eta_n \mathbf{v}_{t,\text{rel}} \right\| \right) t \quad (6)$$

$$\delta = \frac{a^2}{R} - 2\sqrt{\frac{\pi\gamma a}{E}} \quad (7)$$

where the two vertical lines represent the magnitude of the vector, E is the effective Young's modulus given by $E = E_{\text{eff}} = \left(\frac{1-\nu_i^2}{E_i} + \frac{1-\nu_j^2}{E_j} \right)^{-1}$, R the effective radius given by $R = R_{\text{eff}} = \frac{r_i r_j}{r_i + r_j}$, m_{eff} is the effective mass given by $m_{\text{eff}} = \frac{m_i m_j}{(m_i + m_j)}$ and $\delta_{ij} = R_i + R_j - \|\mathbf{r}_{ij}\|$ is the depth of overlap.

The LJ FF is defined by three parameters: ϵ (the depth of the potential well), σ (the distance at which the potential is zero) and r_c (cutoff distance). It works on all types of particles in the simulation box and describes interactions between CBD-CBD, different secondary AM particles and CBD-AM. The JKR FF depends on E (Young's modulus), η_{n0} (damping velocity), ν (Poisson ratios), γ (surface energy density), k_t (tangential stiffness coefficient), $x_{\gamma,t}$ (a scaling coefficient) and μ_t (the tangential friction coefficient). Particularly, the primary particles coalesce together by the JKR force to form the secondary particles and preserve the morphology of the material. The JKR force between CBD-CBD and AM-CBD mainly manifest as a repulsion to avoid excessive overlap. Normally, the particles are not subject to the JKR force until after contact, but this FF allows the particles to have a pull-off force up to $3\pi\gamma R$ after being separated due to hysteresis effects. Here, we choose 135 GPa as Young's modulus value for the NMC111 particles, which is a reasonable value from literature [39–41]. The parameters related to the material properties used in the simulation are shown in Table 1, and the effective parameters between the different materials (E_{eff} , R_{eff} , m_{eff}) are calculated automatically by the LAMMPS software according to the

formulas mentioned above. To simulate the cohesion between the electrode and the current collector (CC, aluminum foil for the NMC111 cathode), we endow the lower wall of the simulated box with a JKR FF. As a result, an attractive force is added between the lower wall and the particles in contact with it. The mass of the particle is used as m_{eff} , and R_{eff} is set to the radius of the particle. When considering the LJ force between different materials, we use the values of $0.8 \times (\epsilon_i + \epsilon_j)$, $0.5 \times (\sigma_i + \sigma_j)$ and $0.5 \times (r_{ci} + r_{cj})$ to calculate ϵ_{ij} , σ_{ij} and $r_{c ij}$ respectively for all possible pairs ij . A simple schematic is shown in Fig. S3. It is worth noting that the FF parameter values are different between primary particles inside each active material particle, and between primary particles belonging to different active material particles. The values of the FF parameter are reported in Table S2.

3. Results and discussion

3.1. μ -XCT data analysis

At the experimental level, μ -XCT is used to investigate the changes in the geometric properties of our *in-house* manufactured electrodes, before and after a 30% compression calendering. The microstructures of both the electrodes are analyzed by μ -XCT, and the obtained data is segmented into biphasic image stacks. The tortuosity factors of the microstructures are calculated using the software TauFactor [42]. It is worth noting that the CBD and pore phases were combined to calculate the porosity and the tortuosity factor since it is not possible to derive the morphology of the nanopores in CBD. At this point, the former is likely to be overstated while the latter is probably underestimated. Furthermore, the sub-volumes with the same dimensions as our model are cropped out from a random location for the same study. Fig. 1A depicts the 3D microstructures of the uncalendered and calendered electrodes. 20 sub-volumes of the same size as our model are randomly cut out and the microstructure parameters are calculated, as illustrated by the hollow points presented in Fig. 1B. Their average value is then compared with the value from our modeling-anticipated microstructures. The sub-volumes that are most comparable to the average value are selected for comparison, which are shown in Fig. 1C. The volume fraction distribution of the two phases (AM and Pores + CBD) in the direction of electrode thickness (standardized) is presented in Fig. 1D. From this, it is evident that the volume fraction of AM in the region near the CC and the electrode surface is lower than the average value, whereas the Pores + CBD displays the opposite trend. This is particularly noticeable for the uncalendered electrode, indicating that the calendering process improves the flatness of the electrode surface. The secondary particle morphologies are then extracted from the μ -XCT data to be transformed into the input of CGMD simulations, and the detailed procedures are explained in the Material and Methods section and the workflow is illustrated in Fig. 2.

3.2. Model and simulation results

Here we simulated three steps of the manufacturing process (slurry formulation, drying and calendering) by using CGMD simulations as implemented in LAMMPS [43,44]. Mixing and coating steps are not simulated explicitly in this study despite the fact that they can have a considerable impact on the ultimate 3D electrode microstructure. In the CGMD simulations, the particle beads that constitute our system can be considered as explicit particle beads, such as the primary AM particles that we generated; or as effective particles encompassing carbon, binder

and solvent in the slurry model, or the effective particle encompassing carbon and binder in the dried electrode model. These particles interact due to the action of the FFs, which must be parameterized to mimic the experimental properties of the system [25,45,46]. In our initial microstructure, the PSD of the secondary AM particles is similar to that of the real AM particles, with a diameter of 2–14 μm . In this work, we simulate two different formulations: 94% NMC - 3% C65 – 3% PVdF (94% AM and 6% CBD in the simulation) and 96% NMC – 2% C65 – 2% PVdF (96% AM and 4% CBD). The simulation consists of 166 AM secondary particles for the 96%–4% electrode and 165 particles for the 94%–6% one. The diameter of CBD particles varies depending on whether the simulation is for the slurry or the dried electrode. For the latter, particles with diameter 1.3 μm are considered, whilst the former includes particles of diameter 6.2 μm , with a density (0.95 g/cm³) corresponding to a 50% nanoporosity. The number of CBD particles is calculated to achieve the required mass according to the formulations. The FFs used in this model for the whole manufacturing process simulation include the Lennard-Jones FF (LJ) and Johnson-Kendall-Roberts model-based Granular FF (JKR), which are available in the LAMMPS software. The actual values of Young's modulus and Poisson's ratio of the material are obtained from the literature [39–41] and utilized as input parameters for the JKR FF. The reader is directed to the Material and Methods section for a more detailed description of the CGMD procedures.

The computational workflow is schematized in Fig. 1. The slurry, dried electrode and calendering simulations (9494 AM particles and 5458 CBD particles for 94%–6% and 10330 AM particles and 3877 CBD particles for 96%–4%) take respectively ~24, ~11 and 9–37 h by using one node (128 GB of RAM) composed of 2 processors (Intel® Xeon® CPU E5-2680 v4 @ 2.40 GHz, 14 cores) on the MatriCS platform (Université de Picardie Jules Verne). The simulation of the slurry starts with an initial box of 80 × 80 × 120 μm^3 with periodic conditions in all three directions. An isothermal-isobaric (NPT) condition at 300 K and 10⁵ Pa is applied. Due to the computational limitations of LAMMPS, we were unable to perform the viscosity simulation as in our previous works [22]. The experimental density values were utilized to validate the outcome of this stage. The comparison of the simulation results and the experimental values are shown in Table 2.

During the drying step, we consider the homogeneous evaporation model [25], in which all the CBD particles of diameter 6.2 μm , containing the solvent, shrink into the solid size, with diameter 1.3 μm , instantaneously. The system is then left to equilibrate. The values of the FF parameters change in drying in order to mimic the phase changes coming from slurry (mimicking a liquid-like behavior) to the ones of the dried electrode (mimicking a solid behavior). The values of the FF parameters are reported in Table S2 of the Supplemental Information. The fundamental difference between the FF parameters of the slurry and the dried electrode is an increase in the attractive and elastic interactions, accounting for stronger particle links due to binder bridges and a greater Young modulus, respectively. In this case, instead of applying periodic boundary conditions in all three directions, a fixed surface is used perpendicular to the z-axis (Cartesian coordinate system). We computed and defined the final thickness of the dried electrode based on its experimental density and porosity and vary the thickness of the entire electrode during the non-equilibrium molecular dynamic simulation. As a result, the electrode thickness decreases from top to bottom (electrode surface to CC). At each time step, the temperature is rescaled in order to maintain the entire simulation at 353 K (80 °C). We compare the results with experimental porosities and tortuosity factors, as well as the values derived from the μ -XCT data for the dried electrodes. For both volumes, we assumed that the CBD phase comprises 50% of nanopores which is below the obtainable spatial resolution and therefore cannot be partitioned out.

Another critical step in the battery manufacturing process is electrode calendering. In LIBs, calendered electrodes result in boosting electronic conductivities and mechanical strengths, which are necessary in order to optimize the volumetric energy and power densities of the

Table 1

Parameters related to the material properties.

	CBD _{liquid}	CBD _{solid}	AM	Aluminum (CC)	Steel (Calendar roll)
E (GPa)	0.0005	2	135	69	200
ν	0.3	0.3	0.3	0.3	0.3

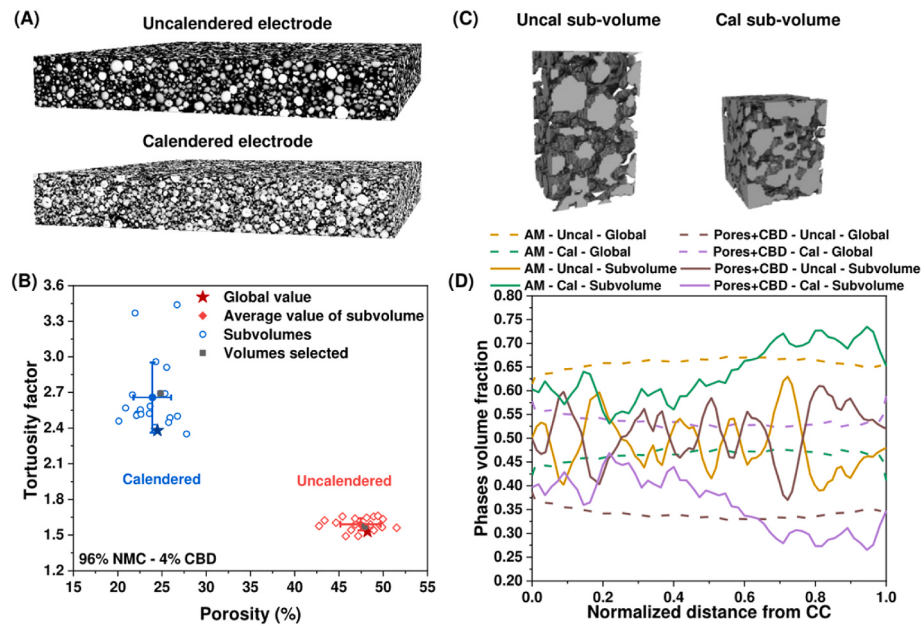


Fig. 1. Quantitative analysis of the μ -XCT data. A: Global 3D microstructures of the uncalendered and calendered electrodes. B: The porosity and tortuosity factor study on the μ -XCT data. C: Subvolumes selected from uncalendered and calendered electrodes, respectively. D: The volume fraction change of the two phases in the direction of the electrode's thickness.

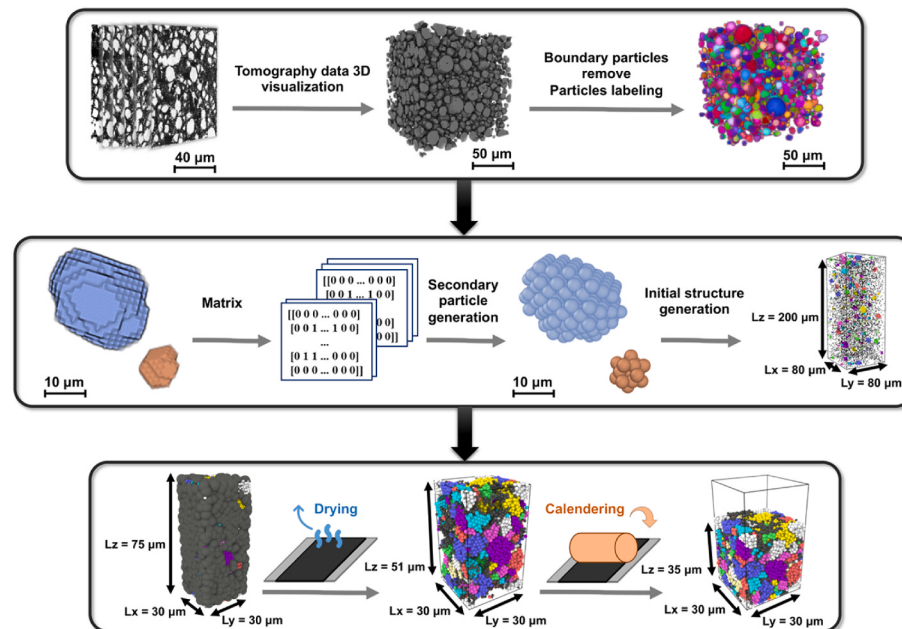


Fig. 2. Schematic representation of the NMC111 AM structure generation procedure. A stack of 2D two-phase maps is reconstructed into a 3D volume, and the individual particles of AM are labeled. The particles cut at the border are removed. Each particle is separately transformed into a 3D matrix and stored in a database sorted by size. The secondary particles with realistic shapes are constructed from the 3D matrix by stacking spherical primary particles, and then randomly picked, rotated and displaced to generate the initial structure. The computational workflow for simulating the manufacturing process of NMC cathode is schematized: slurry, drying and calendering simulations.

Table 2
Comparison of experimental and simulation densities of two slurry compositions with different formulations.

Formulation		Density (g/cm^3)
94% AM – 6% CBD	Experimental value	2.03
	Simulation result	2.04
96% AM – 4% CBD	Experimental value	2.14
	Simulation result	2.18

cells. However, it comes at the risk of collapsing the electrode's pore network at excessive compressions, considerably raising the ionic transport resistance, resulting in decreased rate capabilities and cause

partial exploitation of the AM. Consequently, it is important to analyze the influence of the calendering on the electrode microstructure, which will help choose optimum compression parameters that prevent the aforementioned issues.

In our calendering model, a plane moves downward at a constant speed, compressing the electrode to imitate the actual process of passing the electrode through the calendering rolls. The entire process takes place at a constant temperature of 60 °C, which is consistent with our experiment. During the downward movement of the plane, the particles re-stabilize due to self-reorganization. After reaching the desired degree of compression, the plane is released and the electrode is "relaxed", a process in which the thickness of the electrode is partially regained due to the elasticity of the electrode. The electrode after relaxation is the

outcome of the calendering process. Lastly, in order to eliminate the artificial gaps between the primary particles, while maintaining the volume fraction of the AM unchanged, a dilation-erosion mapping step was used as a post-processing step of the simulation results, as described in the Supplemental Information.

The experimental porosity values are utilized to verify the porosity of the electrode obtained from our simulation, as shown in Fig. 3A, which exhibits a good agreement. Meanwhile, the tortuosity factor values obtained by μ -XCT are used to further validate their microstructures. To ensure a fair comparison, the CBD and pores phases in the electrodes derived from the simulation results are combined into a single phase for calculation. As shown in Fig. 3B, for the uncalendered electrode, the value is in general agreement with the μ -XCT value, whereas for the calendered electrodes, the values are within a tolerable interval. For the two groups of electrodes with different formulations, the porosity-tortuosity factor curves after calendering also show similar trends. Fig. 3C–H depict the distribution of the three phases across the thickness, as well as the predicted dried and calendered electrode microstructures and the corresponding cross-sectional images. The predicted dried electrode has a 50.60% porosity while the calendered electrode has a 23.5% porosity for a 32.7% compression degree. The volume fraction of NMC particles is lower close to the CC and electrode surface, which is related to the elliptical shape of the secondary particles. Such a distribution is in agreement with the μ -XCT results of dried electrodes studied by Zhang et al. [10]. It is obvious that the porosity reduces and the distance between the secondary particles gradually decreases during calendering. Also, the distribution of AM along the thickness direction is more homogeneous, As seen by the fact that the volume fraction (brown curves in Fig. 3D and G) becomes less disrupted as the compression degree increases. Fig. 3E and H show a cross-sectional view of the

distribution of AM of various sizes. Additional information about the phase fractions for different calendering degrees is shown in the Supplemental Information, which shows an increase in the flatness of the electrode surface with the degree of calendering.

Continuing the analysis of the resulting microstructural models, we turn our attention to the porosity distribution. Here, a watershed-based algorithm (Avizo) is used to segment the pore space into individually labeled pore-fragments. A Pore Network Model (PNM) is then used to analyze these individual pores. Although the pores present diverse shapes, they are approximated as spheres. An equivalent radius is calculated to represent the size and to examine the size distribution. To account for the voxel size of the μ -XCT data (which represents the lowest limit of our analysis), only pores with a radius greater than 1 μm are included in the statistics. The connectivity of the pore network is assessed by connecting neighboring pairs of individual pores with throats. The cross-sectional area of such throats is proportional to the interfacial area shared by the corresponding pair of pores. Fig. 4 shows a comparison between the PNMs of our simulated (CGMD) and experimentally (μ -XCT) obtained microstructures for the 96% AM – 4% CBD electrode. Simple visual inspection reveals that the simulated microstructures present more complex pore networks than the ones from μ -XCT, most likely due to the smaller voxel sizes used to map the results from the CGMD simulations back into a voxel representation of the microstructures, allowing for a higher resolution analysis of the PNM. In both cases, the calendering process results in an overall reduction of the number of large pores, where the average radius of the pores in the simulated (experimental) calendered microstructures is reduced from 2.99 μm to 2.28 μm (from 3.76 μm to 2.16 μm), respectively. Additionally, a larger amount of smaller-sized pores appear in comparison to the uncalendered electrodes. The pore size distribution along the

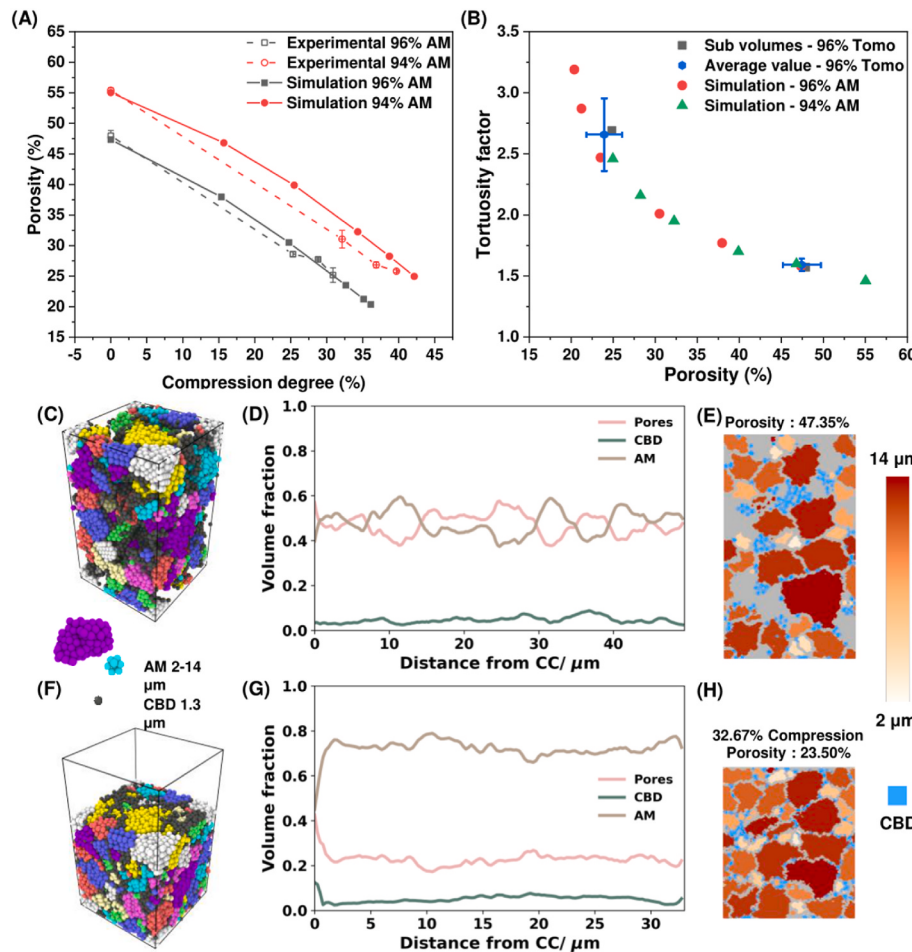


Fig. 3. Results validation and microstructure study. A: Comparison between experimental and simulated porosity for both electrode compositions as a function of compression degree. B: Tortuosity factor (τ) as a function of the porosity during the simulated calendering and comparison with μ -XCT data. C and F: The 3D structure resulting from the calendering model. D and G: Pore, CBD and AM volume distribution along the thickness direction, represented by black, red and blue curves respectively. E and H: Cross-sectional view for the electrodes. Panels c through h correspond to the 96% NMC – 4% CBD formulation. The blue represents the CBD and the red from light to dark represents different sizes of AM. (For interpretation of the references to color in this figure legend, the reader is referred to the Web version of this article.)

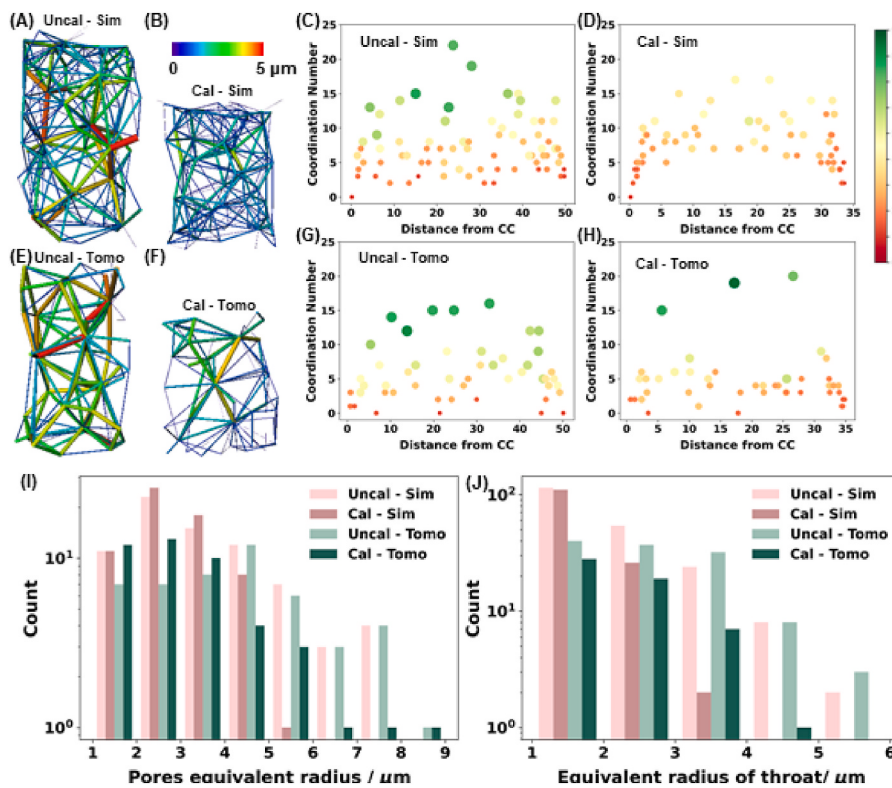


Fig. 4. Pore network study on uncalendered and calendered electrodes from the model for 96% AM – 4% CBD electrode. A, B and F: Color-coded throats between different pores for uncalendered (A, B) and calendered (B, F) electrodes coming from simulations (A, B) and μ -XCT experiments (E, F). The color bar represents the radius of each throat. C, D, G and H: Size and coordination number of each pore in the PNM as a function of their position along the electrode's thickness. The color bar indicates the equivalent diameter of the pores. I: Global pore size distribution. J: Global throat size distribution.

thickness direction and the corresponding number of pores connected to them for these four microstructures are depicted in Fig. 4C, D, G and H. Upon calendering, the larger pores are reduced and replaced by smaller ones with a lower coordination number, which explains the increase in the electrode's tortuosity factor. Since the μ -XCT volumes are arbitrarily cropped from the large electrode, this pore evolution analysis is not applicable. The cross-sectional sizes of the throats, which give an indication of the mass transfer efficiency between neighboring pores, likewise decrease dramatically in the calendered electrodes. The quantitative results in Fig. 4J indicate that narrower and more numerous channels appear after calendering.

A novel feature of our modeling approach is that it allows us to trace the deformation of individual secondary particles. The commercial software GeoDict (Math 2 Market) [47] is used to fit the individual particles into ellipses, which are then evaluated for Krumbein sphericity ($\sqrt[3]{bc}/a^2$, where a , b , and c are the sizes of the axes of the ellipsoid). Fig. 5 gives the distribution of the Krumbein sphericities in the microstructure before and after the calendering process. It can be seen that the sphericities alter owing to calendering, but the peak is always around 0.7–0.8. This deformation of particles has already been reported in the experimental literature [48]. In addition, our model offers the possibility to study the variation of particle orientation during calendering, as described in detail in the Supplemental Information.

Furthermore, a comparison of the real particle shapes model and our previous model with spherical AM particles [25] has also been achieved. In the two models, the electrodes with the same formulation (94% NMC – 6% CBD), particle size distribution are simulated. The CBD size for both cases is 1.3 μ m. The tortuosity factor values of the electrodes have been compared. As we can see from the Fig. S7, by taking CBD into consideration, the outcomes of the new approach display relative high tortuosity factors, which is attributed by the heterogeneity of the AM shape and its distribution. Compared with Fig. 3B, the phase volume used for the calculation is reduced and the tortuosity factor value is significantly higher due to the inclusion of CBD. It is worth pointing out that the true tortuosity factor value of the electrode should be in between, due to the

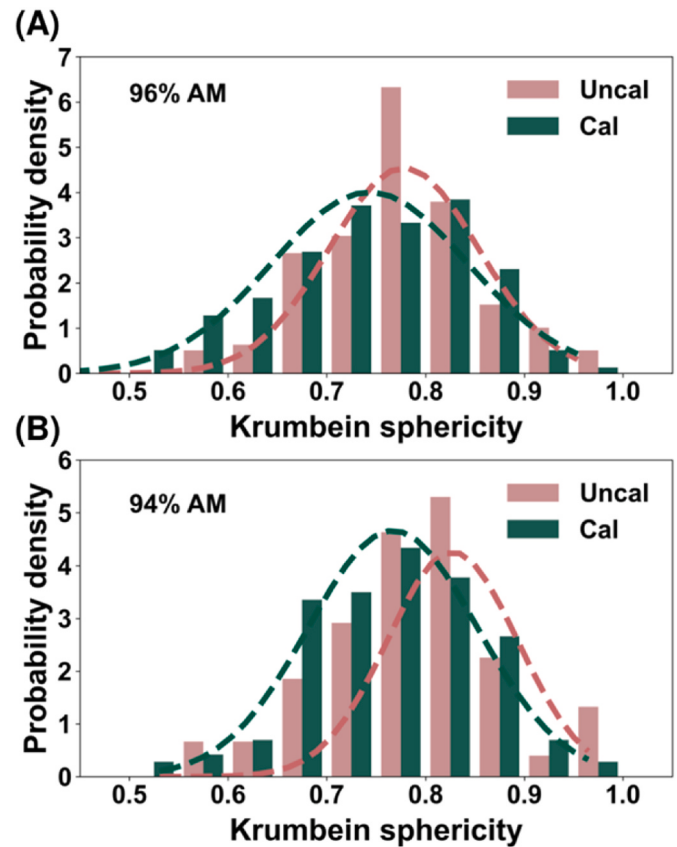


Fig. 5. The study on deformation of secondary particles. A and B: The distribution of Krumbein sphericity value in the uncalendered and calendered electrode for two different formulations.

fact that the volume of the CBD contains 50% of the nanopores. It is clear that the introduction of real particles shapes improves our understanding of the true architecture of the electrode, as does the availability of tracking particle deformation and orientation changes, both of which cannot be captured by the spherical model.

4. Conclusion

To summarize, we have developed a set of models of the LIB electrode manufacturing process that incorporate AM particle morphologies arising from μ -XCT characterizations. The aim of this work is to digitally predict the impact of the electrode manufacturing process parameters on the electrode microstructure. The new approach leads to a more realistic simulation of electrode slurries, their drying and the calendering, allowing for a more in-depth investigation of the effect of manufacturing on the electrode heterogeneity. The experimental findings of the μ -XCT of the electrode before and after the calendering are compared with the model results, showing reasonable agreement. The new model captures the variation of the electrode microstructure during the manufacturing process, as well as the effect of the manufacturing parameters on the electrode heterogeneity. Furthermore, it enables tracking the AM particles deformation and orientation changes during the calendering process. We observed that the secondary particles have suffered from modest deformations at high pressure due to the mechanical properties of NMC111, and there is no evident pattern of orientation shift. For subsequent research, this method will be extended to other electrode materials with lower hardness, such as graphite. Through our experiments and the literature, the cracking due to the calendering is a very interesting phenomenon to study as well. This phenomenon is happening at a scale smaller than the secondary particles sizes considered in our model and can be linked to the degree of particle deformation. This is something that we are investigating in our group and will be the subject of future work by us. Finally, the approach presented in this article is fully compatible with the ARTISTIC online computational workflow [49], and as such, the results from this model can be used for pursuant electrolyte infiltration, electrochemical simulation studies or for other purposes.

FUNDING

J.X., A.C.N., C. L. and A.A.F. acknowledge the European Union's Horizon 2020 research and innovation program for the funding support through the European Research Council (grant agreement 772873, "ARTISTIC" project). A.A.F. acknowledges Institut Universitaire de France for the support. F.M.Z., O.A. and A.A.F. acknowledge the European Union's Horizon 2020 research and innovation program under grant agreement No 957189 (BIG-MAP).

CRediT authorship contribution statement

Jiahui Xu: Conceptualization, Methodology, Software, Validation, Visualization, Investigation, Writing - original draft. **Alain C. Ngandjong:** Conceptualization, Methodology, Software, Writing – original draft. **Chaoyue Liu:** Software, Visualization. **Franco M. Zanotto:** Validation, Writing – review & editing. **Oier Arcelus:** Conceptualization, Software, Writing – review & editing. **Arnaud Demortière:** Supervision, Writing - review & editing. **Alejandro A. Franco:** Conceptualization, Methodology, Supervision, Funding acquisition, Project administration, Resources, Writing - review & editing.

Declaration of competing interest

The authors declare that they have no known competing financial interests or personal relationships that could have appeared to influence the work reported in this paper.

Data availability

The data and model will be made available via our ARTISTIC project online calculator: <https://www.erc-artistic.eu/computational-portal>.

Acknowledgments

Prof. Alejandro A. Franco's research team acknowledges the Matrics HPC platform from Université de Picardie-Jules Verne for the support and for hosting and managing the ARTISTIC dedicated nodes used for the calculations reported in this manuscript. The team acknowledges Markus Osenberg and Prof. Ingo Manke from Institute of Applied Materials, Helmholtz-Zentrum Berlin für Materialien und Energie GmbH (Germany) for the tomography data collection.

Appendix A. Supplementary data

Supplementary data to this article can be found online at <https://doi.org/10.1016/j.jpowsour.2022.232294>.

References

- [1] Y. Yang, E.G. Okonkwo, G. Huang, S. Xu, W. Sun, Y. He, On the sustainability of lithium ion battery industry – a review and perspective, Energy Storage Mater. 36 (2021) 186–212, <https://doi.org/10.1016/j.ensm.2020.12.019>.
- [2] F.M. Zanotto, D.Z. Dominguez, E. Ayerbe, I. Boyano, C. Burmeister, M. Duquesnoy, M. Eisentraeger, J.F. Montaño, A. Gallo-Bueno, L. Gold, F. Hall, N. Kaden, B. Muerners, L. Otaegui, Y. Reynier, S. Stier, M. Thomitzek, A. Turetskyy, N. Vallin, J. Wessel, X. Xu, J. Abbasov, A.A. Franco, Data Specifications for Battery Manufacturing Digitalization: Current Status, Challenges, and Opportunities, Batter. Supercaps. n/a (n.d.) e202200224. <https://doi.org/10.1002/batt.202200224>.
- [3] J. Li, J. Fleetwood, W.B. Hawley, W. Kays, From materials to cell: state-of-the-art and prospective technologies for lithium-ion battery electrode processing, Chem. Rev. 122 (2022) 903–956, <https://doi.org/10.1021/acs.chemrev.1c00565>.
- [4] W.B. Hawley, J. Li, Electrode manufacturing for lithium-ion batteries—analysis of current and next generation processing, J. Energy Storage 25 (2019), 100862, <https://doi.org/10.1016/j.est.2019.100862>.
- [5] A. Kraysberg, Y. Ein-Eli, Conveying advanced Li-ion battery materials into practice the impact of electrode slurry preparation skills, Adv. Energy Mater. 6 (2016), 1600655, <https://doi.org/10.1002/aenm.201600655>.
- [6] The impact of particle size and shape on battery electrode slurry formation | Malvern Panalytical, (n.d.). <https://www.malvernpanalytical.com/es/learn/knowledge-center/application-notes/an170103batteryslurryparticlessize>. (Accessed 9 May 2022).
- [7] D. Grießl, A. Adam, K. Huber, A. Kwade, Effect of the slurry mixing process on the structural properties of the anode and the resulting fast-charging performance of the lithium-ion battery cell, J. Electrochem. Soc. 169 (2022), 020531, <https://doi.org/10.1149/1945-7111/ac4cdb>.
- [8] W.B. Hawley, J. Li, Beneficial rheological properties of lithium-ion battery cathode slurries from elevated mixing and coating temperatures, J. Energy Storage 26 (2019), 100994, <https://doi.org/10.1016/j.est.2019.100994>.
- [9] Y.S. Zhang, N.E. Courtier, Z. Zhang, K. Liu, J.J. Bailey, A.M. Boyce, G. Richardson, P.R. Shearing, E. Kendrick, D.J.L. Brett, A review of lithium-ion battery electrode drying: mechanisms and metrology, Adv. Energy Mater. (2021), 2102233, <https://doi.org/10.1002/aenm.202102233>.
- [10] Y.S. Zhang, J.J. Bailey, Y. Sun, A.M. Boyce, W. Dawson, C.D. Reynolds, Z. Zhang, X. Lu, P. Grant, E. Kendrick, P.R. Shearing, D.J.L. Brett, Applications of advanced metrology for understanding the effects of drying temperature in the lithium-ion battery electrode manufacturing process, J. Mater. Chem. A. 10 (2022) 10593–10603, <https://doi.org/10.1039/D2TA00861K>.
- [11] A. Shodiev, M. Chouchane, M. Gaberscek, O. Arcelus, J. Xu, H. Oularbi, J. Yu, J. Li, M. Morcrette, A.A. Franco, Deconvoluting the benefits of porosity distribution in layered electrodes on the electrochemical performance of Li-ion batteries, Energy Storage Mater. 47 (2022) 462–471, <https://doi.org/10.1016/j.ensm.2022.01.058>.
- [12] H. Zheng, L. Tan, G. Liu, X. Song, V.S. Battaglia, Calendering effects on the physical and electrochemical properties of Li[Ni1/3Mn1/3Co1/3]O2 cathode, J. Power Sources 208 (2012) 52–57, <https://doi.org/10.1016/j.jpowsour.2012.02.001>.
- [13] C. Meyer, H. Bockholt, W. Haselrieder, A. Kwade, Characterization of the calendering process for compaction of electrodes for lithium-ion batteries, J. Mater. Process. Technol. 249 (2017) 172–178, <https://doi.org/10.1016/j.jmatprotec.2017.05.031>.
- [14] X. Gao, W. Lu, J. Xu, Unlocking multiphysics design guidelines on Si/C composite nanostructures for high-energy-density and robust lithium-ion battery anode, Nano Energy 81 (2021), 105591, <https://doi.org/10.1016/j.nanoen.2020.105591>.
- [15] P. Pietsch, V. Wood, X-ray tomography for lithium ion battery research: a practical guide, Annu. Rev. Mater. Res. 47 (2017) 451–479, <https://doi.org/10.1146/annurev-matsci-070616-123957>.

- [16] X. Lu, A. Bertei, D.P. Finegan, C. Tan, S.R. Daemi, J.S. Weaving, K.B. O'Regan, T.M. M. Heenan, G. Hinds, E. Kendrick, D.J.L. Brett, P.R. Shearing, 3D microstructure design of lithium-ion battery electrodes assisted by X-ray nano-computed tomography and modelling, *Nat. Commun.* 11 (2020) 2079, <https://doi.org/10.1038/s41467-020-15811-x>.
- [17] L. Zielke, T. Hutzenlaub, D.R. Wheeler, I. Manke, T. Arlt, N. Paust, R. Zengerle, S. Thiele, A combination of X-ray tomography and carbon binder modeling: reconstructing the three phases of LiCoO₂ Li-ion battery cathodes, *Adv. Energy Mater.* 4 (2014), 1301617, <https://doi.org/10.1002/aenm.201301617>.
- [18] T. Nguyen, J. Villanova, Z. Su, R. Tucoulou, B. Fleutot, B. Delobel, C. Delacourt, A. Demortière, 3D quantification of microstructural properties of LiNi_{0.5}Mn_{0.3}Co_{0.2}O₂ high-energy density electrodes by X-ray holographic nano-tomography, *Adv. Energy Mater.* 11 (2021), 2003529, <https://doi.org/10.1002/aenm.202003529>.
- [19] T. Lombardo, M. Duquesnoy, H. El-Bousyid, F. Åren, A. Gallo-Bueno, P.B. Jørgensen, A. Bhowmik, A. Demortière, E. Ayerbe, F. Alcaide, M. Reynaud, J. Carrasco, A. Grimaud, C. Zhang, T. Vegge, P. Johansson, A.A. Franco, Artificial intelligence applied to battery research: hype or reality?, *Chem. Rev.* 122, 12 (2022) 10899–10969, doi.org/10.1021/acs.chemrev.1c00108 .
- [20] Z. Su, E. Decencière, T.-T. Nguyen, K. El-Amiry, V. De Andrade, A.A. Franco, A. Demortière, Artificial neural network approach for multiphase segmentation of battery electrode nano-CT images, *Npj Comput. Mater.* 8 (2022) 30, <https://doi.org/10.1038/s41524-022-00709-7>.
- [21] ERC artistic : home, artistic. (n.d.). <http://www.erc-artistic.eu/>. (Accessed 9 May 2022).
- [22] T. Lombardo, J. Hoock, E.N. Primo, A.C. Ngandjong, M. Duquesnoy, A.A. Franco, Accelerated optimization methods for force-field parametrization in battery electrode manufacturing modeling, *Batter. Supercaps.* 3 (2020) 721–730, <https://doi.org/10.1002/batt.202000049>.
- [23] A.C. Ngandjong, A. Rucci, M. Maiza, G. Shukla, J. Vazquez-Arenas, A.A. Franco, Multiscale simulation platform linking lithium ion battery electrode fabrication process with performance at the cell level, *J. Phys. Chem. Lett.* 8 (2017) 5966–5972, <https://doi.org/10.1021/acs.jpclett.7b02647>.
- [24] T. Lombardo, A.C. Ngandjong, A. Belhcen, A.A. Franco, Carbon-binder migration: a three-dimensional drying model for lithium-ion battery electrodes, *Energy Storage Mater.* 43 (2021) 337–347, <https://doi.org/10.1016/j.ensm.2021.09.015>.
- [25] A.C. Ngandjong, T. Lombardo, E.N. Primo, M. Chouchane, A. Shodiev, O. Arcelus, A.A. Franco, Investigating electrode calendering and its impact on electrochemical performance by means of a new discrete element method model: towards a digital twin of Li-Ion battery manufacturing, *J. Power Sources* 485 (2021), 229320, <https://doi.org/10.1016/j.jpowsour.2020.229320>.
- [26] A. Shodiev, E. Primo, O. Arcelus, M. Chouchane, M. Osenberg, A. Hilger, I. Manke, J. Li, A.A. Franco, Insight on electrolyte infiltration of lithium ion battery electrodes by means of a new three-dimensional-resolved lattice Boltzmann model, *Energy Storage Mater.* 38 (2021) 80–92, <https://doi.org/10.1016/j.ensm.2021.02.029>.
- [27] A. Shodiev, F.M. Zanotto, J. Yu, M. Chouchane, J. Li, A.A. Franco, Designing electrode architectures to facilitate electrolyte infiltration for lithium-ion batteries, *Energy Storage Mater.* 49 (2022) 268–277, <https://doi.org/10.1016/j.ensm.2022.03.049>.
- [28] A. Shodiev, M. Duquesnoy, O. Arcelus, M. Chouchane, J. Li, A.A. Franco, Machine learning 3D-resolved prediction of electrolyte infiltration in battery porous electrodes, *J. Power Sources* 511 (2021), 230384, <https://doi.org/10.1016/j.jpowsour.2021.230384>.
- [29] M. Chouchane, A. Rucci, T. Lombardo, A.C. Ngandjong, A.A. Franco, Lithium ion battery electrodes predicted from manufacturing simulations: assessing the impact of the carbon-binder spatial location on the electrochemical performance, *J. Power Sources* 444 (2019), 227285, <https://doi.org/10.1016/j.jpowsour.2019.227285>.
- [30] M. Duquesnoy, T. Lombardo, M. Chouchane, E.N. Primo, A.A. Franco, Data-driven assessment of electrode calendering process by combining experimental results, in silico mesostructures generation and machine learning, *J. Power Sources* 480 (2020), 229103, <https://doi.org/10.1016/j.jpowsour.2020.229103>.
- [31] M. Duquesnoy, C. Liu, D.Z. Dominguez, V. Kumar, E. Ayerbe, A.A. Franco, Machine learning-assisted multi-objective optimization of battery manufacturing from synthetic data generated by physics-based simulations. <http://arxiv.org/abs/2205.01621>, 2022. (Accessed 31 May 2022).
- [32] M. Nikpour, N. Barrett, Z. Hillman, A.I. Thompson, B.A. Mazzeo, D.R. Wheeler, A model for investigating sources of Li-ion battery electrode heterogeneity: Part I. Electrode drying and calendering processes, *J. Electrochim. Soc.* 168 (2021), 060547, <https://doi.org/10.1149/1945-7111/ac0bf1>.
- [33] A. Mistry, T. Heenan, K. Smith, P. Shearing, P.P. Mukherjee, Asphericity can cause nonuniform lithium intercalation in battery active particles, *ACS Energy Lett.* 7 (2022) 1871–1879, <https://doi.org/10.1021/acsenergylett.2c00870>.
- [34] F. Wilde, M. Ogureck, I. Greving, J.U. Hammel, F. Beckmann, A. Hipp, L. Lottermoser, I. Khokhriakov, P. Lytaev, T. Dose, H. Burmester, M. Müller, A. Schreyer, Micro-CT at the imaging beamline P05 at PETRA III, *AIP Conf. Proc.* 1741 (2016), <https://doi.org/10.1063/1.4952858>, 030035.
- [35] I. Arganda-Carreras, V. Kaynig, C. Rueden, K.W. Elceir, J. Schindelin, A. Cardona, H. Sebastian Seung, Trainable Weka Segmentation: a machine learning tool for microscopy pixel classification, *Bioinformatics* 33 (2017) 2424–2426, <https://doi.org/10.1093/bioinformatics/btx180>.
- [36] Avizo software | materials characterization software - FR, (n.d.). <https://www.thermofisher.com/fr/fr/home/electron-microscopy/products/software-em-3d-vis/avizo-software.html>. (Accessed 8 June 2022).
- [37] J.E. Lennard-Jones, Cohesion, *Proc. Phys. Soc.* 43 (1931) 461–482, <https://doi.org/10.1088/0959-5309/43/5/301>.
- [38] K.L. Johnson, K. Kendall, A.D. Roberts, D. Tabor, Surface energy and the contact of elastic solids, *Proc. Roy. Soc. Lond. Math. Phys. Sci.* 324 (1971) 301–313, <https://doi.org/10.1098/rspa.1971.0141>.
- [39] R. Xu, Y. Yang, F. Yin, P. Liu, P. Cloetens, Y. Liu, F. Lin, K. Zhao, Heterogeneous damage in Li-ion batteries: experimental analysis and theoretical modeling, *J. Mech. Phys. Solid.* 129 (2019) 160–183, <https://doi.org/10.1016/j.jmps.2019.05.003>.
- [40] R. Xu, H. Sun, L.S. de Vasconcelos, K. Zhao, Mechanical and structural degradation of LiNi_xMn_yCo_zO₂ cathode in Li-ion batteries: an experimental study, *J. Electrochim. Soc.* 164 (2017), <https://doi.org/10.1149/2.1751713jes>, A3333–A3341.
- [41] L.S. de Vasconcelos, R. Xu, J. Li, K. Zhao, Grid indentation analysis of mechanical properties of composite electrodes in Li-ion batteries, *Extreme Mech. Lett.* 9 (2016) 495–502, <https://doi.org/10.1016/j.eml.2016.03.002>.
- [42] S.J. Cooper, A. Bertei, P.R. Shearing, J.A. Kilner, N.P. Brandon, TauFactor: an open-source application for calculating tortuosity factors from tomographic data, *SoftwareX* 5 (2016) 203–210, <https://doi.org/10.1016/j.softx.2016.09.002>.
- [43] A.P. Thompson, H.M. Aktulga, R. Berger, D.S. Bolintineanu, W.M. Brown, P. S. Crozier, A. Kohlmeyer, S.G. Moore, T.D. Nguyen, R. Shan, M.J. Stevens, J. Tranchida, C. Trott, S.J. Plimpton, Lammmps - a flexible simulation tool for particle-based materials modeling at the atomic, meso, and continuum scales, *Comput. Phys. Commun.* 271 (2022), 108171, <https://doi.org/10.1016/j.cpc.2021.108171>.
- [44] LAMMPS molecular dynamics simulator, (n.d.). <https://www.lammps.org/>. (Accessed 9 May 2022).
- [45] A. Rucci, A.C. Ngandjong, E.N. Primo, M. Maiza, A.A. Franco, Tracking variabilities in the simulation of Lithium Ion Battery electrode fabrication and its impact on electrochemical performance, *Electrochim. Acta* 312 (2019) 168–178, <https://doi.org/10.1016/j.electacta.2019.04.110>.
- [46] M.M. Forouzan, C.-W. Chao, D. Bustamante, B.A. Mazzeo, D.R. Wheeler, Experiment and simulation of the fabrication process of lithium-ion battery cathodes for determining microstructure and mechanical properties, *J. Power Sources* 312 (2016) 172–183, <https://doi.org/10.1016/j.jpowsour.2016.02.014>.
- [47] GeoDict applications - math2Market, (n.d.). <https://www.geodict.com/geodict-software/geodict-applications.html>. (Accessed 8 June 2022).
- [48] X. Lu, S.R. Daemi, A. Bertei, M.D.R. Kok, K.B. O'Regan, L. Rasha, J. Park, G. Hinds, E. Kendrick, D.J.L. Brett, P.R. Shearing, Microstructural evolution of battery electrodes during calendering, *Joule* 4 (2020) 2746–2768, <https://doi.org/10.1016/j.joule.2020.10.010>.
- [49] T. Lombardo, F. Caro, A.C. Ngandjong, J.-B. Hoock, M. Duquesnoy, J.C. Delepine, A. Ponchelet, S. Doison, A.A. Franco, The ARTISTIC online calculator: exploring the impact of lithium-ion battery electrode manufacturing parameters interactively through your browser, *Batter. Supercaps.* 5 (2022), e202100324, <https://doi.org/10.1002/batt.202100324>.